

Supporting Information

Non-Monotonic Size-Dependent Exciton Radiative Lifetime in CsPbBr₃ Nanocrystals

Abdullah S. Abbas^{1,†}, *Daniel Chabeda*², *Daniel Weinberg*^{2,3}, *David T. Limmer*^{2,3,7}, *Eran Rabani*^{2,3,8}, *A. Paul Alivisatos*^{1,2,3,4,5,6,§,*}

¹Department of Materials Science and Engineering, University of California, Berkeley, Berkeley, California 94720, United States

²Department of Chemistry, University of California, Berkeley, Berkeley, California 94720, United States

³Materials Sciences Division, Lawrence Berkeley National Laboratory, Berkeley, California 94720, United States

⁴Department of Chemistry, The University of Chicago, Chicago, Illinois 60637, United States

⁵Pritzker School of Molecular Engineering, The University of Chicago, Chicago, Illinois 60637, United States

⁶James Franck Institute, The University of Chicago, Chicago, Illinois 60637, United States

⁷Kavli Energy NanoScience Institute, Berkeley, California 94720, United States

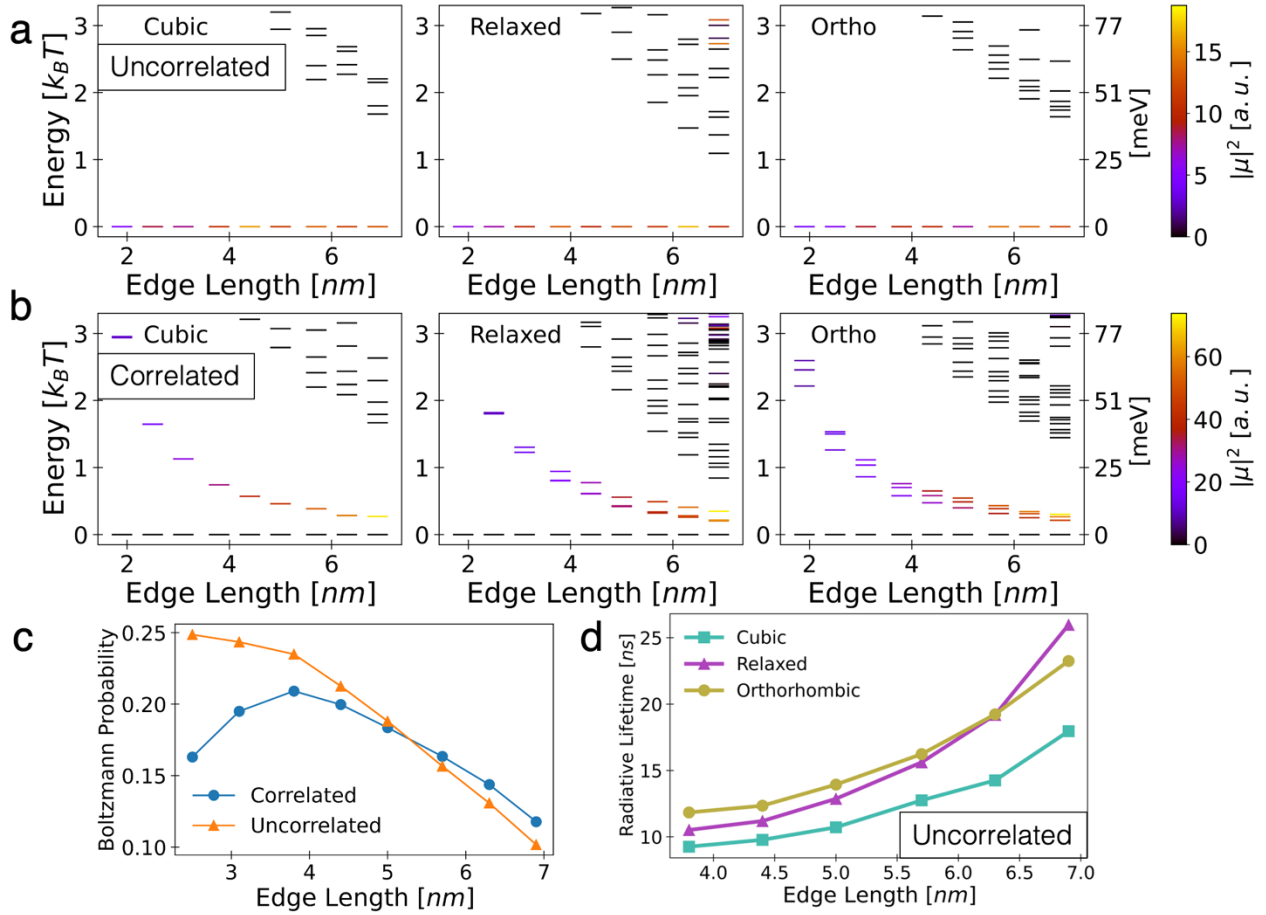
⁸The Raymond and Beverly Sackler Center of Computational Molecular and Materials Science, Tel Aviv University, Tel Aviv 69978, Israel

Present addresses:

[†]Department of Chemistry, The University of Chicago, Chicago, Illinois 60637, United States

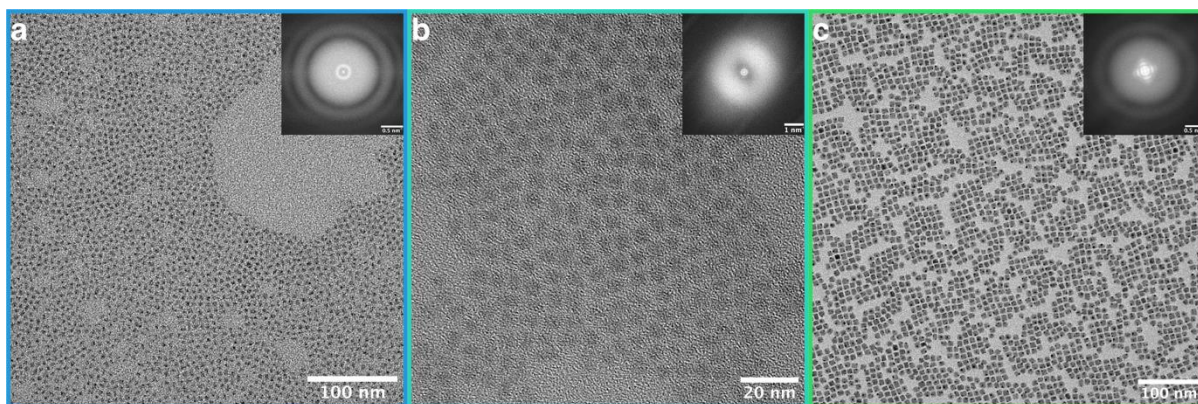
[§]Department of Chemistry and Pritzker School of Molecular Engineering, The University of Chicago, Chicago, Illinois 60637, United States

*To whom correspondence may be addressed: paul.alivisatos@uchicago.edu

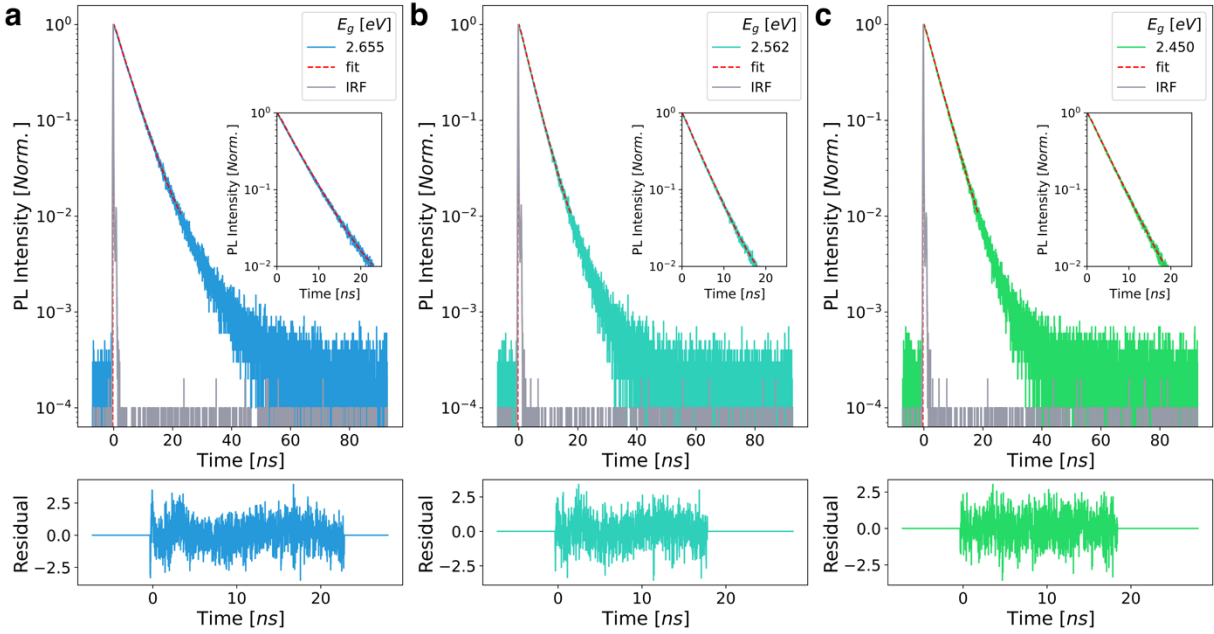


Supplementary Figure 1: Contrasting Size Dependent Radiative Lifetime Trend Without Electron-Hole Correlation. Exciton energy level diagrams as a function of CsPbI₃ nanocube edge length for (a) uncorrelated and (b) correlated excitons. Uncorrelated excitons are taken as a product of an electron and hole state, and correlated excitons are obtained by solving the BSE. For uncorrelated electron-hole pairs, the lowest energy states are quadruply degenerate bright states, with higher lying dim states becoming thermally accessible for larger systems in which the DOS is increased. The fine structure changes when we solve the BSE and include electron-hole correlations. The lowest energy state is a dim singlet below a manifold of bright triplet excitons. (c) Size-dependent Boltzmann population of the lowest energy bright state for uncorrelated (orange triangles) and correlated (blue circles) excitons. For small NCs, there is opposing size dependent behavior. Thermal population of higher lying states decreases the emissive ground state

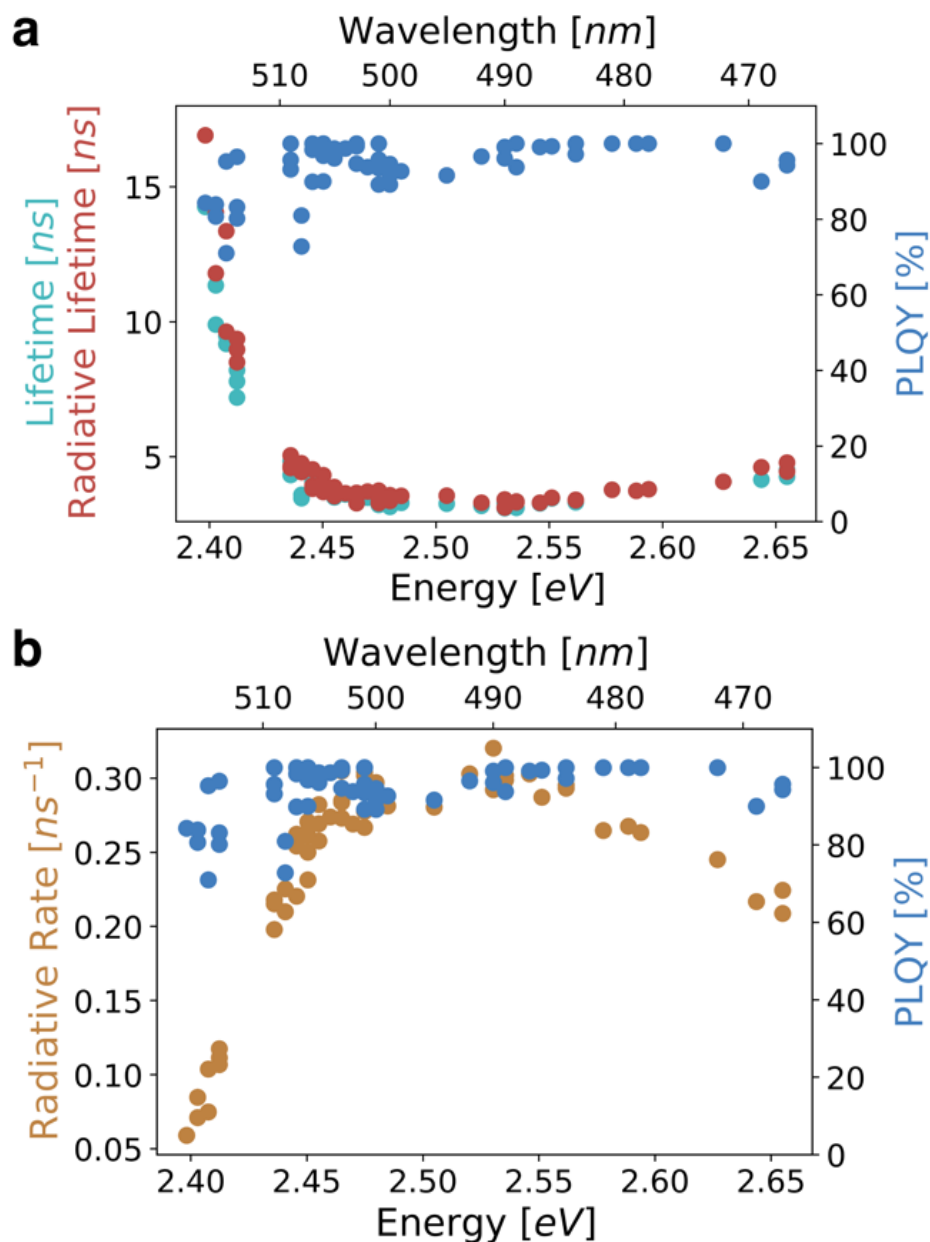
population for uncorrelated excitons, while for correlated excitons the emissive triplet state increases in population for larger NCs, until the inflection point where thermal population of higher lying dim states decreases the triplet population. **(d)** Predicted radiative lifetimes of uncorrelated excitons in cubic (teal squares), relaxed (purple triangles), and orthorhombic (gold circles) nanocrystals increase monotonically due to decreased Boltzmann population of the emissive manifold. Contrastingly, for correlated excitons, reduced confinement in larger NCs lowers the energy of the bright triplet states with respect to the dim ground state, increasing the Boltzmann population of emissive states and decreasing the lifetime (Fig. 5).



Supplementary Figure 2: Transmission electron microscopy (TEM) characterization of CsPbBr_3 nanocrystals. TEM images of three selected nanocrystals sizes in (a) strong, (b) intermediate, and (c) weak quantum confinement regime with their corresponding Fast Fourier Transform (FFT).



Supplementary Figure 3: Time-resolved photoluminescence (TRPL) characterization. **a**, depicts TRPL decays, deconvoluted with instrument response function (IRF), with the initial two decades fitted to a monoexponential function for nanocrystal sizes within **(a)** strong, **(b)** intermediate, and **(c)** weak quantum confinement regime. Each plot includes the residuals showing the goodness of the fit.



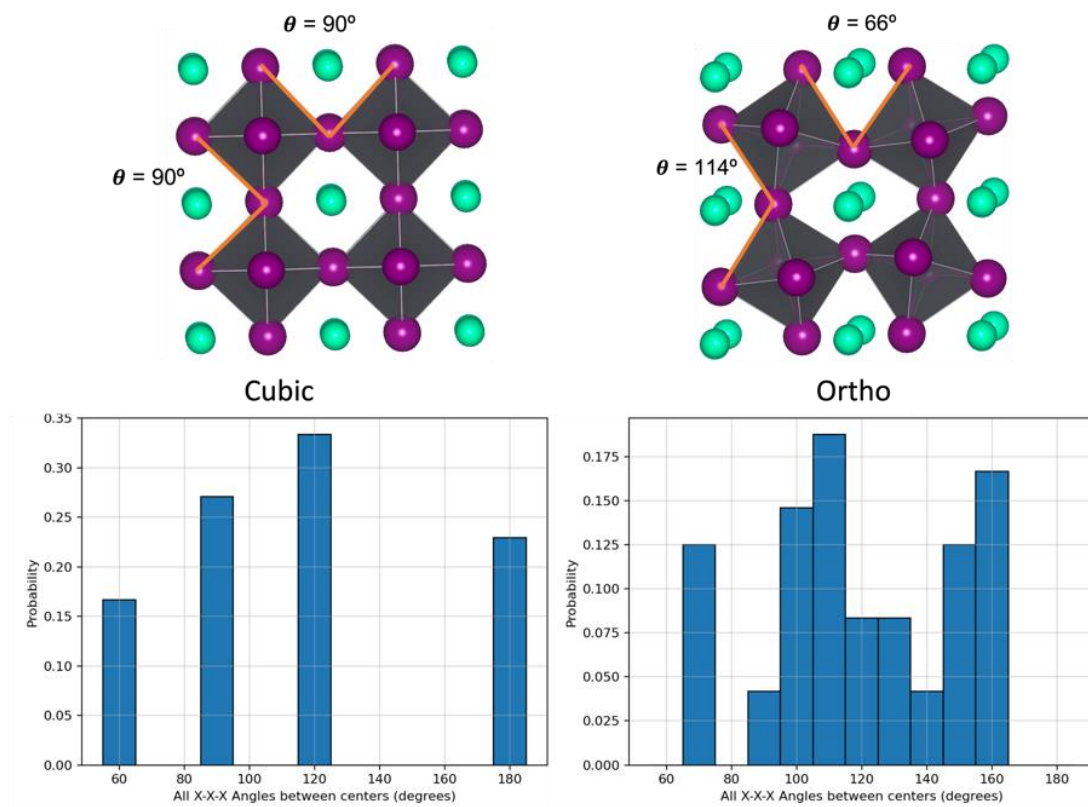
58

59 **Supplementary Figure 4: Size-dependent radiative lifetimes and rates of CsPbBr₃**

60 **nanocrystals.** Varying nanocrystals spanning further in the weak confinement regime illustrating

61 extended (a) radiative lifetimes and reduced (b) radiative rates.

62

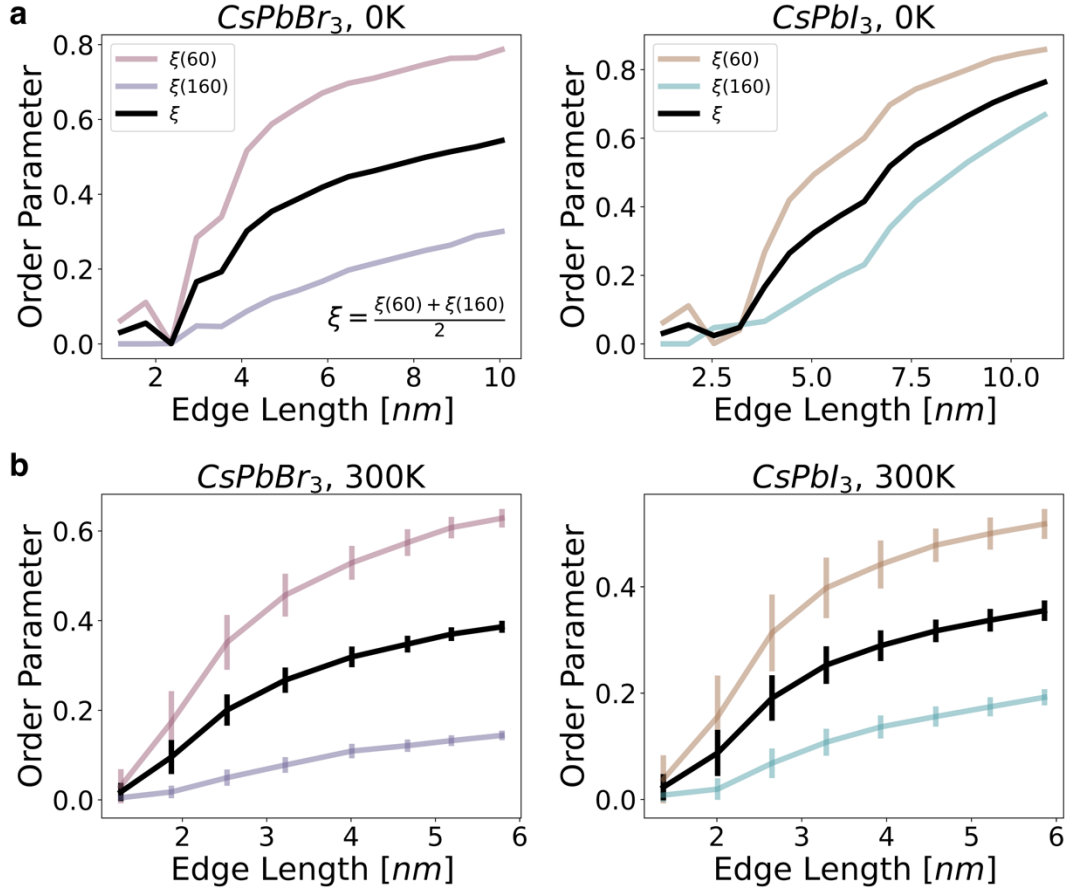


63

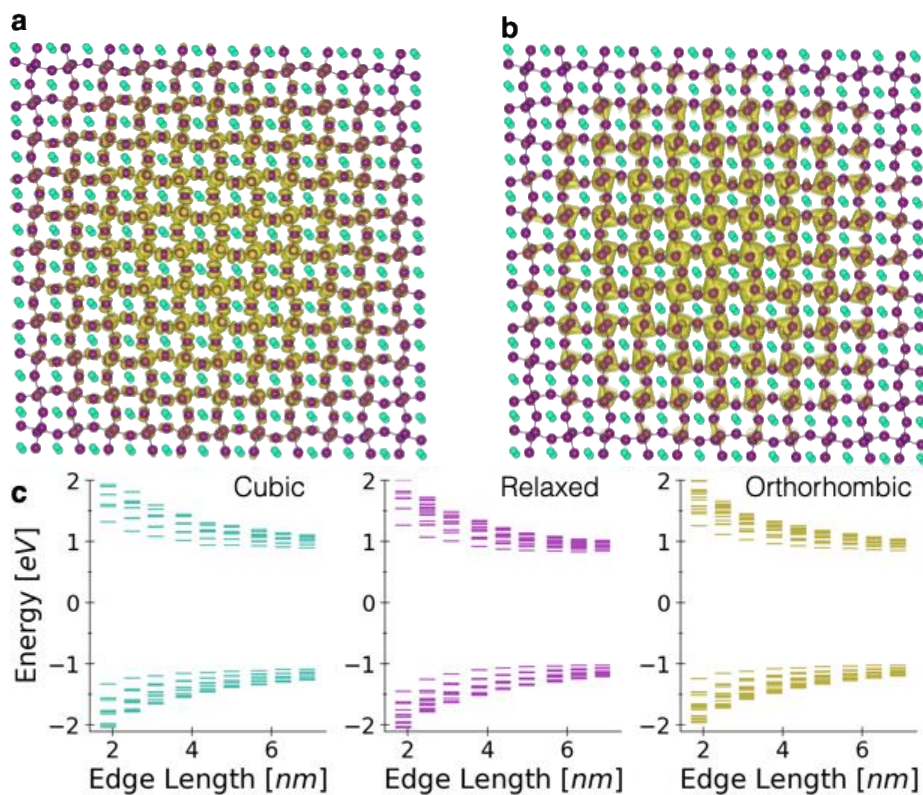
64 **Supplementary Figure 5: Cubic vs orthorhombic CsPbBr₃ structure.** Probability distribution

65 of X-X-X angles in ideal (a) cubic and (b) orthorhombic CsPbBr₃ structure. In the cubic symmetry,

66 the 60° angle is distinctly prominent, while 160° angle occurs only in the orthorhombic symmetry.



Supplementary Figure 6: Size-dependent order parameters for CsPbX₃ (X = Br, I) at 0K and 300K from MD simulations. Comparison of order parameter for CsPbBr₃ and CsPbI₃ nanocrystals with varying sizes at (a) 0 K and (b) 300 K. Both perovskites initially exhibit cubic symmetry in smaller sizes, then transition into orthorhombic symmetry as the nanocrystal size increases. Error bars denote the variance of the order parameter due to fluctuations in the 100 sampled geometries over the simulation.



75

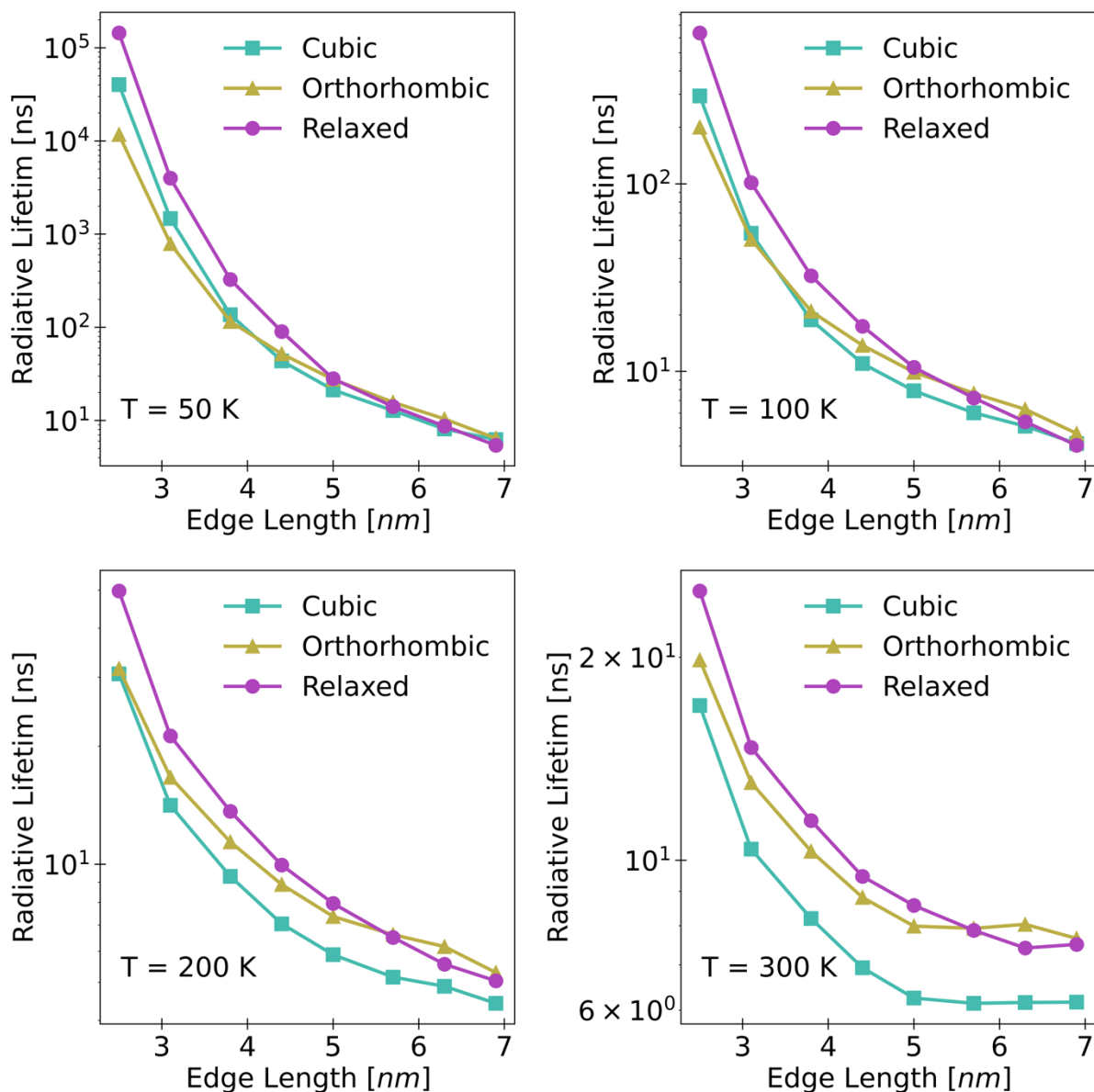
76 **Supplementary Figure 7: Quasiparticle states in perovskite NCs.** Representative particle

77 densities from our atomistic semi-empirical pseudopotential method for the (a) valence band edge

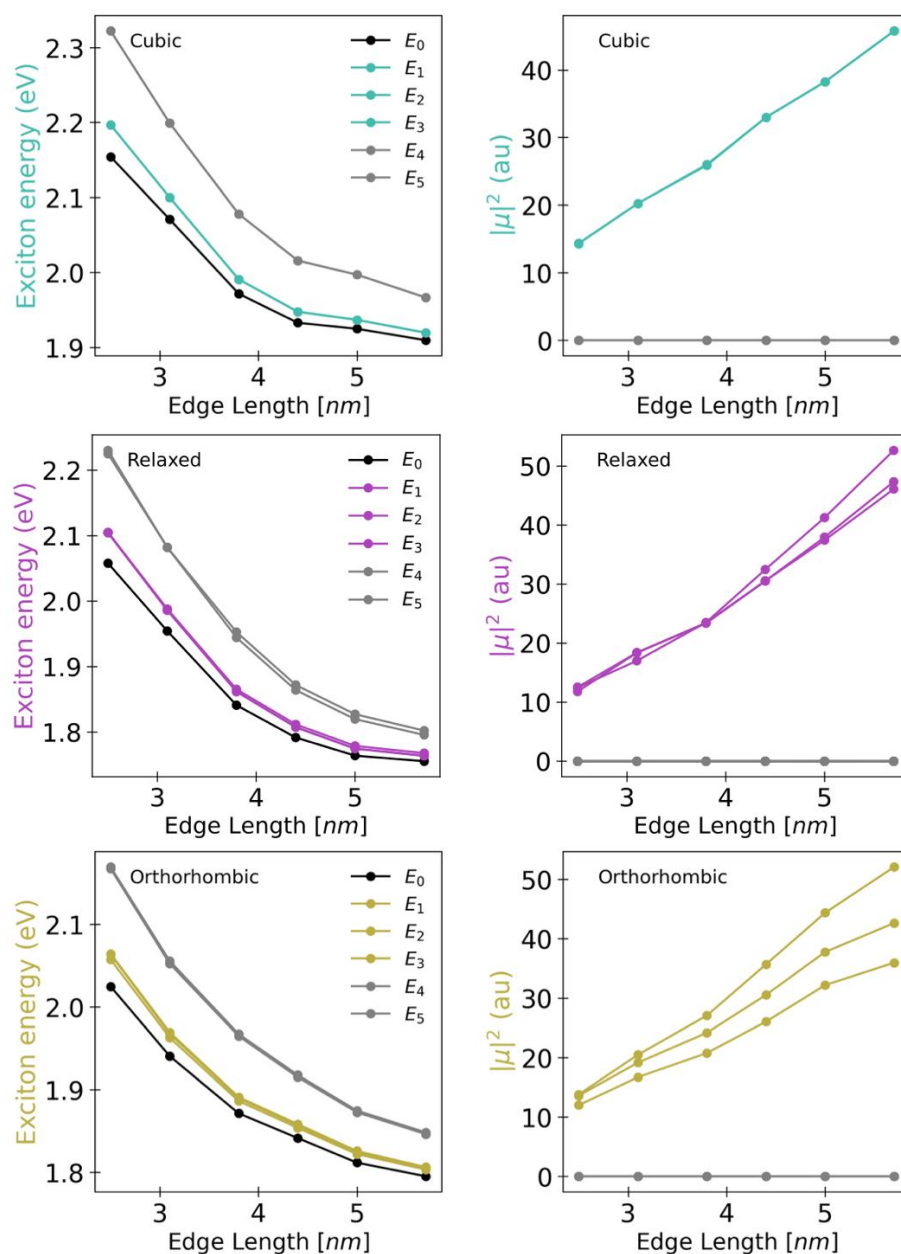
78 (HOMO) and (b) conduction band edge (LUMO) states of a 6.9 nm orthorhombic CsPbI₃

79 nanocrystal. (c) Quasiparticle energies of 32 hole and 32 electron states as a function of size for

80 cubic, relaxed, and orthorhombic CsPbI₃ nanocrystals.



Supplementary Figure 8: Size Dependent Radiative Lifetime Across Different Temperatures. Radiative lifetimes of halide perovskites as a function of temperature calculated at (a) 50 K, (b) 100 K, (c) 200 K, and (d) 300 K, demonstrating a transition from an exponential trend observed for low temperatures to a non-monotonic trend for higher temperatures, indicating that the dim states became thermally accessible.



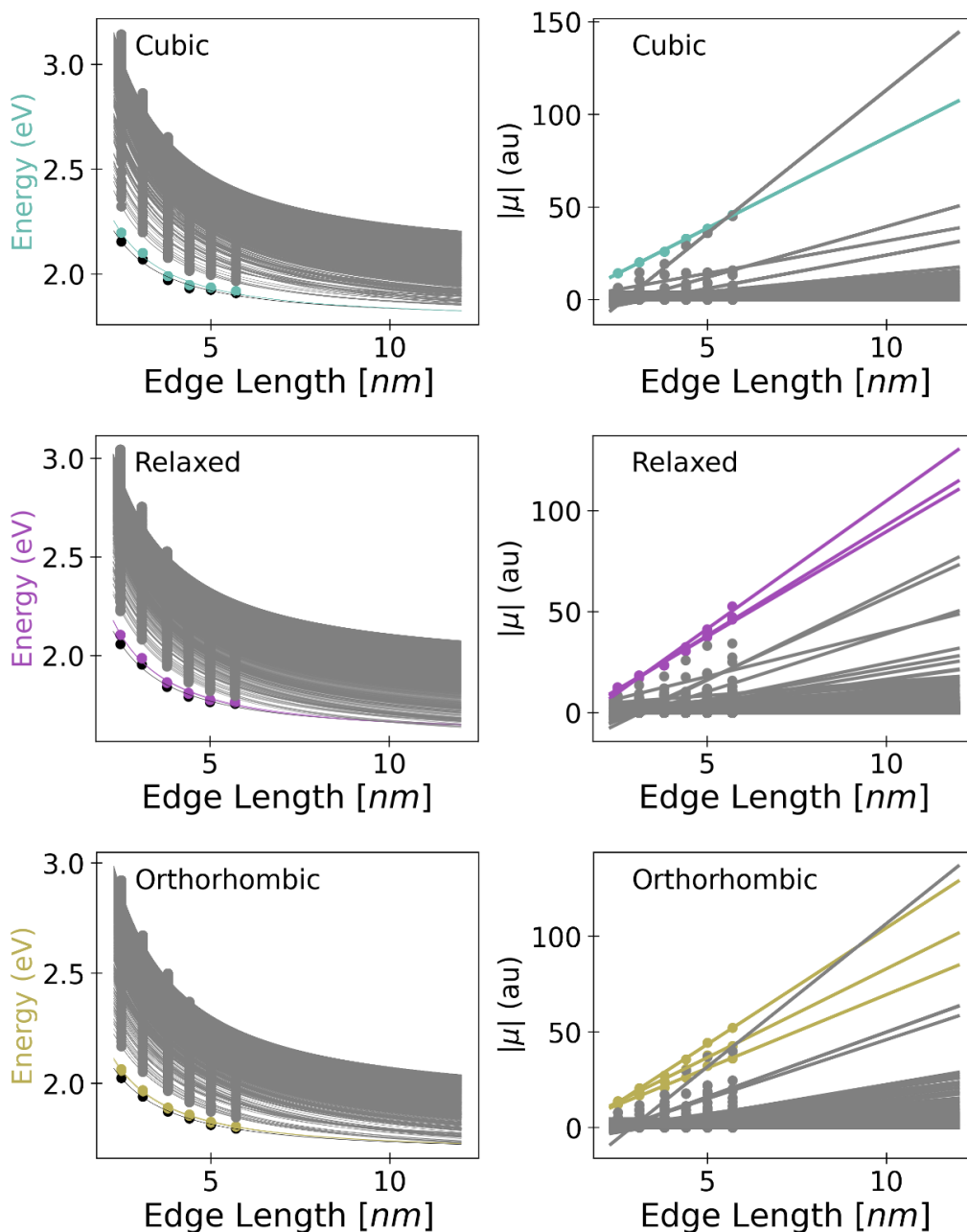
88

89 **Supplementary Figure 9: Representative energy and squared transition dipole fits.** Size-

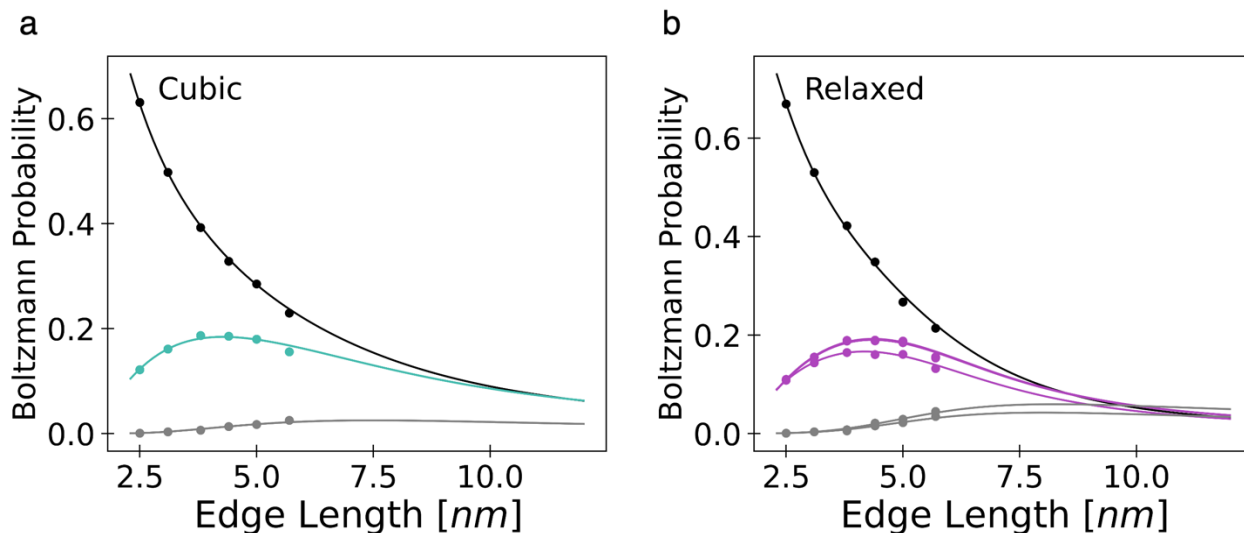
90 dependent energies (left) and squared transition dipole moments (right) of the six lowest energy

91 exciton states for CsPbI₃ NCs ranging from 2.5 – 5.7 nm edge lengths. The excitons were computed

92 in the BSE framework with an electron-hole basis of a few thousand pair states.



Supplementary Figure 10: All exciton energy and squared transition dipole fits. Fits as a function of size for the energies (left) and oscillator strengths (right) of the first 1024 excitons in CsPbI₃ NCs with various crystal structures. The energy of each exciton level was fit to a polynomial $E(x) = a(x - b)^{-c} + d$, where c was found to range from 1.2 to 1.4. The squared transition dipole moments were fitted to a linear function $u(x) = a*x + b$. No other properties were fitted.



Supplementary Figure 11: Size-dependent Boltzmann probabilities. Size-dependent Boltzmann probabilities for the lowest exciton state (top, black), bright triplet states (color), and first two high-lying dim states (bottom, grey). The marked points are the calculated values from atomistic simulations, and the lines are extrapolated from fits of the exciton energies vs. size. These are the corresponding companions to main text Fig. 5b for the cubic and relaxed crystal structures. As the NC edge length increases, population of the lowest exciton decreases due to the decreasing dark-bright gap. As the particle sizes increase further, closing of the bright-dim gap leads to depopulation of the bright triplets, generating a non-monotonic Boltzmann population.

Generating nanocrystal configurations

The procedure for generating NCs is taken from Weinberg et al.¹ In summary, the cubic and orthorhombic nanocrystal (NC) structures were generated by cutting the bulk crystal structures.² The cut was made along the 100 facets for cubic structures and the 110 and 001 facets for orthorhombic structures. The cuts were made to ensure cesium and iodine surface termination, and all lead-iodide octahedra were complete. This finite structure has a modified stoichiometry compared to bulk and is not charge neutral. To reduce charge imbalance, we rescale the charge of the surface cesium atoms to make the structure charge neutral. The modified charges of the surface cesium atoms, q_{surf} are

$$q_{surf} = -\frac{N_{Pb}q_{Pb} + N_Iq_I + N_{Cs}q_{Cs}}{N_{surf}}$$

where N_α, q_α are the number and charge respectively of each atom type, $\alpha = \{Cs, Pb, I\}$. The values of these charges are listed in Supplementary Table 1.

Relaxed nanocrystal structures were generated by conjugate gradient minimization of a previously parametrized³ Lennard-Jones/Coulomb pair potential, u_{ij} , between atoms i and j with the form

$$u_{ij} = \frac{q_i q_j}{4\pi\epsilon_0 r} + 4\epsilon_{ij} \left[\left(\frac{\sigma_{ij}}{r} \right)^{12} - \left(\frac{\sigma_{ij}}{r} \right)^6 \right], r < r_c$$

where i, j index the atom type, ϵ_0 is the vacuum electric permittivity, and r_c is defined so that all pairwise interactions are computed for the finite system. The Lennard-Jones parameters ϵ and σ are tabulated in Supplementary Table 1. The interatomic pair parameters can be derived using the following combining rules, $\epsilon_{ij} = \sqrt{\epsilon_i \epsilon_j}$ and $\sigma_{ij} = (\sigma_i + \sigma_j)/2$. For each size of nanocrystal, we take the unrelaxed orthorhombic structure as an initial configuration. The eight corner Cs atoms were found to be unstable on conjugate gradient relaxation, so those atoms were removed for all structures. Minimizations are performed using the LAMMPS package.⁴

132 **Supplementary Table 1.** Force field parameters.

	ϵ (eV)	$\sigma(\text{\AA})$	q (e)
CsPbBr ₃			
Cs	0.5784	2.927	0.86
Pb	0.01071	2.524	1.03
Br	0.01023	4.129	-0.63
CsPbI ₃			
Cs	0.07728	3.584	0.86
Pb	0.001086	3.210	0.85
I	0.06389	4.014	-0.57

133

134 **Computing single particle electronic structure and excitonic states**

135 The procedure used here was employed without modification from the methodology of Weinberg
 136 et al reported in their Supplementary Information.¹ The electronic structure was computed using a
 137 semiempirical pseudopotential approach,^{5–8} in which each atom is assigned a local, nonlocal, and
 138 spin–orbit potential derived by fitting to bulk band structures of the cubic and orthorhombic
 139 geometries. The single-particle Hamiltonian is given by:

140
$$\hat{H} = \hat{T} + \sum_{\alpha} [\hat{V}_{loc}^{\alpha} + \hat{V}_{nonloc}^{\alpha} + \hat{V}_{SO}^{\alpha}]$$

141 where \hat{T} is the kinetic energy operator, \hat{V}_{loc}^{α} is the spherically symmetric local pseudopotential
 142 around atom α , $\hat{V}_{nonloc}^{\alpha}$ accounts for angular momentum dependent corrections, and \hat{V}_{SO}^{α} accounts
 143 for spin-orbit coupling. The local potential is fit in reciprocal space,

144
$$\tilde{v}_{loc}^{\alpha}(q) = a_0^{\alpha} \frac{q - a_1^{\alpha}}{a_2^{\alpha} \exp(a_3^{\alpha} q^2) - 1}$$

145 and subsequent Fourier transform gives the representation in real space,

146
$$V_{loc}^{\alpha} = v_{loc}^{\alpha}(|\mathbf{r} - \mathbf{R}_{\alpha}|).$$

147 The angular momentum dependent nonlocal and spin-orbit potentials give corrections for electrons
 148 in p -type orbitals:

149
$$V_{nonloc}^{\alpha} = [a_4^{\alpha} \exp(-|\mathbf{r} - \mathbf{R}_{\alpha}|^2) + a_5^{\alpha} \exp(-(|\mathbf{r} - \mathbf{R}_{\alpha}| - \rho)^2)] P_{l=1}^{\alpha}$$

150
$$V_{SO}^{\alpha} = a_6^{\alpha} \exp\left(\frac{-|\mathbf{r} - \mathbf{R}_{\alpha}|^2}{w^2}\right) \mathbf{L}^{\alpha} \cdot \mathbf{S} P_{l=1}^{\alpha}$$

151 Where $P_{l=1}^{\alpha}$ is the projector onto the $l = 1$ angular momentum subspace around atom α , ρ is a
 152 shift of 1.5 Bohr, \mathbf{L}^{α} is the electron orbital angular momentum vector operator around atom α , \mathbf{S}
 153 is the electron spin vector operator, and w is a width of 0.7 Bohr. The non-local operators were
 154 implemented via a modified Kleinman-Bylander representation.^{9–11} All parameters $a_i^{\alpha}, i \in \{0,6\}$
 155 are given in Supplementary Table 2 for both cubic and orthorhombic geometries. For relaxed
 156 nanocrystal structures, no single bulk phase exactly matches the local atomic environment, so the
 157 pseudopotentials were linearly interpolated between the fitted cubic and orthorhombic potentials
 158 based on the local Pb–I–Pb bond angles. Select eigenstates of this Hamiltonian near the band
 159 edge were obtained using the filter diagonalization technique on a real-space grid with 0.5 Bohr
 160 grid spacing, sufficient to converge all operators.^{12–15}

161 **Supplementary Table 2.**

Iodine	Orthorhombic	Cubic	Lead	Orthorhombic	Cubic
a_0	117.89162750	113.75644925	a_0	97.86083166	88.83030750
a_1	2.12591587	2.14135468	a_1	2.25710305	2.60529157
a_2	2.91148249	2.84227140	a_2	3.71951773	4.28692327
a_3	0.58243028	0.56706414	a_3	0.55872538	0.51950186
a_4	0.16631532	0.04515637	a_4	1.40412238	1.06405744
a_5	-0.02486412	0.00220169	a_5	-0.01566674	-0.00808029
a_6	2.23037552	3.03441874	a_6	7.94721141	7.78990812

163 To describe optical excitations, excitonic states were computed by solving the Bethe–Salpeter
 164 Equation (BSE) in the Tamm-Dancoff approximation.¹⁶ The correlated exciton wavefunction is
 165 expanded in the basis of electron–hole pair states,

$$166 \quad |\psi_n\rangle = \sum_{a,i} c_{a,i}^n |a, i\rangle,$$

167 Where indices a, b refer to electron states, indices i, j refer to hole states, $|a, i\rangle$ is a non-
 168 interacting product state. The coefficients $c_{a,i}^n$ are determined by the eigenvalue equation

$$169 \quad (E_n - \Delta\varepsilon_{a,i})c_{a,i}^n = \sum_{b,j} (K_{ai;b j}^d + K_{ai;b j}^x)c_{b,j}^n$$

170 Where E_n is the exciton energy, $\Delta\varepsilon_{a,i}$ is the energy difference between electron a and hole i . The
 171 electron hole interaction kernel, $K_{ai;b j}^d + K_{ai;b j}^x$, has two parts: the direct interaction K^d describes
 172 the Coulomb attraction between the electron-hole pair, while the exchange interaction K^x
 173 controls the details of the excitonic singlet-triplet splitting. The direct interaction is calculated
 174 using the screened Coulomb operator, $W(|\mathbf{r} - \mathbf{r}'|)$, with a static dielectric constant $\epsilon = 6.1$.

$$175 \quad K_{ai;b j}^d = -\int d\mathbf{x}d\mathbf{x}' \phi_a^*(\mathbf{x})\phi_j^*(\mathbf{x}')W(|\mathbf{r} - \mathbf{r}'|)\phi_i(\mathbf{x}')\phi_b(\mathbf{x})$$

176 The exchange interaction is computed with the bare Coulomb operator as

$$177 \quad K_{ai;b j}^x = \int d\mathbf{x}d\mathbf{x}' \phi_a^*(\mathbf{x})\phi_j^*(\mathbf{x}')v(|\mathbf{r} - \mathbf{r}'|)\phi_b(\mathbf{x}')\phi_i(\mathbf{x})$$

178 where $\phi_a(\mathbf{x}) = \langle \mathbf{r}, \sigma | a \rangle$ and $\phi_i(\mathbf{x}) = \langle \mathbf{r}, \sigma | i \rangle$ are electron and hole single particle orbitals in
 179 real space.

180 A central quantity in our work is the exciton transition dipole moment, computed as

181
$$\boldsymbol{\mu}_n = \sum_{a,i} c_{a,i}^n \langle a | \hat{\boldsymbol{\mu}} | i \rangle,$$

182 where $\boldsymbol{\mu}_n$ is the exciton transition dipole moment vector and $\hat{\boldsymbol{\mu}}$ is the electric dipole moment
183 operator on the single particle states.

184

185

186

187

- 188 1. Weinberg, D., Park, Y., Limmer, D. T. & Rabani, E. Size-dependent lattice symmetry
189 breaking determines the exciton fine structure of perovskite nanocrystals. *Nano Letters* **23**,
190 4997–5003 (2023).
- 191 2. Sutton, R. J. *et al.* Cubic or Orthorhombic? Revealing the Crystal Structure of Metastable
192 Black-Phase CsPbI₃ by Theory and Experiment. *ACS Energy Lett.* **3**, 1787–1794 (2018).
- 193 3. Bischak, C. G. *et al.* Liquid-like Interfaces Mediate Structural Phase Transitions in Lead
194 Halide Perovskites. *Matter* **3**, 534–545 (2020).
- 195 4. Thompson, A. P. *et al.* LAMMPS - a flexible simulation tool for particle-based materials
196 modeling at the atomic, meso, and continuum scales. *Computer Physics Communications* **271**,
197 108171 (2022).
- 198 5. Wang, L. W. & Zunger, A. Electronic Structure Pseudopotential Calculations of Large
199 (.apprx.1000 Atoms) Si Quantum Dots. *J. Phys. Chem.* **98**, 2158–2165 (1994).
- 200 6. Wang, L.-W. & Zunger, A. Pseudopotential calculations of nanoscale CdSe quantum dots.
201 *Physical review. B, Condensed matter* **53**, 9579–9582 (1996).
- 202 7. Rabani, E., Hetényi, B., Berne, B. J. & Brus, L. E. Electronic properties of CdSe nanocrystals
203 in the absence and presence of a dielectric medium. *The Journal of Chemical Physics* **110**,
204 5355–5369 (1999).
- 205 8. Williamson, A. J. & Zunger, A. Pseudopotential study of electron-hole excitations in colloidal
206 free-standing InAs quantum dots. *Phys. Rev. B* **61**, 1978–1991 (2000).
- 207 9. Kleinman, L. & Bylander, D. M. Efficacious Form for Model Pseudopotentials. *Phys. Rev.*
208 *Lett.* **48**, 1425–1428 (1982).

- 209 10. King-Smith, R. D., Payne, M. C. & Lin, J. S. Real-space implementation of nonlocal
210 pseudopotentials for first-principles total-energy calculations. *Phys. Rev. B* **44**, 13063–13066
211 (1991).
- 212 11. Blöchl, P. E. Generalized separable potentials for electronic-structure calculations. *Phys.*
213 *Rev. B* **41**, 5414–5416 (1990).
- 214 12. Neuhauser, D. Circumventing the Heisenberg principle: A rigorous demonstration of
215 filter-diagonalization on a LiCN model. *J. Chem. Phys.* **100**, 5076–5079 (1994).
- 216 13. Neuhauser, D. Bound state eigenfunctions from wave packets: Time→energy resolution.
217 *J. Chem. Phys.* **93**, 2611–2616 (1990).
- 218 14. Wall, M. R. & Neuhauser, D. Extraction, through filter-diagonalization, of general
219 quantum eigenvalues or classical normal mode frequencies from a small number of residues
220 or a short-time segment of a signal. I. Theory and application to a quantum-dynamics model.
221 *The Journal of Chemical Physics* **102**, 8011–8022 (1995).
- 222 15. Toledo, S. & Rabani, E. Very Large Electronic Structure Calculations Using an Out-of-
223 Core Filter-Diagonalization Method. *Journal of Computational Physics* **180**, 256–269 (2002).
- 224 16. Rohlfing, M. & Louie, S. G. Electron-hole excitations and optical spectra from first
225 principles. *Phys. Rev. B* **62**, 4927–4944 (2000).
- 226